

Estimation of the OSCAT Spatial Response Function Using Island Targets

Joshua P. Bradley and David G. Long, *Fellow, IEEE*

Abstract—Originally designed for wind velocity estimation over the ocean, scatterometers have been applied to weather forecasting, global climatological studies, and monitoring of large-scale human interaction on the planet. Launched in September of 2009, the Oceansat-2 Ku-band scatterometer (OSCAT) is an excellent candidate for continuing the data time series begun with QuikSCAT, which was the SeaWinds scatterometer flown on the QuikSCAT mission 1999–2009. Some processing algorithms require knowledge of the spatial response function (SRF) of the scatterometer. With limited knowledge of OSCAT implementation, and thus its SRF, a procedure is developed for estimating the SRF. The estimation procedure uses scatterometer measurements over islands to invert the radar equation. A mathematical model is developed that reduces the solution to rank-reduced least-squares estimation. The geographic sampling region is discussed, and a simulation is performed to verify the efficacy of the method, while also providing guidelines for island choice and the number of singular values used in rank reduction. The utility of OSCAT SRF estimates is demonstrated through the construction of an enhanced-resolution radar backscatter image over the Amazon rainforest.

Index Terms—Oceansat-2 scatterometer, remote sensing, scatterometry, spatial response function (SRF).

I. INTRODUCTION

A SCATTEROMETER is an active radar device that collects normalized radar backscatter (σ°) measurements over the Earth. The advent of spaceborne scatterometers has opened the door to more accurate weather forecasting, scientific studies of global climatological phenomena, and monitoring of large-scale human interaction on the planet. Originally intended to estimate wind speed and direction over the ocean, scatterometers have since been utilized to estimate soil moisture [1]–[3], detect polar sea ice extent [4]–[8], track icebergs [9], monitor global vegetation [10]–[14], and map deep sea oil spills [15], among others [16], [17].

On September 23, 2009, the Indian Space Research Organization (ISRO) launched the Oceansat-2 satellite into orbit with a pencil beam Ku-band scatterometer (OSCAT). The satellite orbits about the Earth's poles in a sun-synchronous orientation. The design and orbit geometry are similar to QuikSCAT—the SeaWinds scatterometer of the QuikSCAT

mission—making it an excellent candidate for continuing the resolution-enhanced product data time series that began in 1999. For many resolution-enhanced products, knowledge of the spatial response function (SRF) is required to enhance the utility of scatterometer data, such as ultrahigh-resolution wind retrieval (UHR Winds) [18], scatterometer image reconstruction (SIR) [19], and more [20]–[22]. Creation of resolution-enhanced products was simplified for QuikSCAT by computing and tabulating its SRF [23]. With limited knowledge of the SRF of OSCAT, we desire to estimate it for use in the creation of climate products.

In this paper, a method of estimating the OSCAT SRF using natural land targets is presented. Pertinent background information is provided in Section II, followed by the derivation of the SRF in Section III. The estimation problem is set up in Section IV and mathematical models are proposed to obtain a solution. The geographic sampling region is discussed in Section V, including a description of how the Earth σ° scene is modeled. A simulation process designed to test the efficacy of the proposed estimation scheme and optimize for certain unknowns is discussed in Section VI. Empirical results are presented in Section VII, followed by conclusions in Section VIII.

II. BACKGROUND

OSCAT is a dual-pencil-beam scatterometer employing a 1-m dish antenna which transmits and receives a horizontally polarized inner beam and a vertically polarized outer beam at 13.5 GHz. Its inner and outer beams are at incidence angles of 49° and 57° , respectively, and are transmitted alternately at a pulse repetition frequency (PRF) of 96.5 Hz per beam. It rotates about the Earth in a 2-day exact-repeat sun-synchronous polar orbit while tracing out a helix on the Earth by conically scanning about the nadir vector at a rate of 20.5 rpm, synchronous with the PRF [24]. Fig. 1(a) illustrates the OSCAT measurement geometry compared with that of QuikSCAT. The design characteristics of both instruments are given in Table I.

OSCAT transmits and receives using a linear frequency-modulated (LFM) chirp. The radar echo from the surface undergoes signal processing to compute an estimate of the σ° of the surface illuminated by the antenna. The 3-dB footprint illuminated by the antenna is elliptically shaped with dimensions of approximately 26.8×45.1 km for the inner beam and 29.7×68.5 km for the outer beam. Measurements computed from the antenna footprint are termed “eggs.” In addition, range compression is performed on board to separate the

Manuscript received September 27, 2013; revised March 6, 2013; accepted March 27, 2013. Date of publication May 13, 2013; date of current version December 24, 2013.

The authors are with the Microwave Earth Remote Sensing Laboratory, Brigham Young University, Provo, UT 84602 USA (e-mail: bjoshuap@gmail.com; long@ee.byu.edu).

Color versions of one or more of the figures in this paper are available online at <http://ieeexplore.ieee.org>.

Digital Object Identifier 10.1109/TGRS.2013.2256429

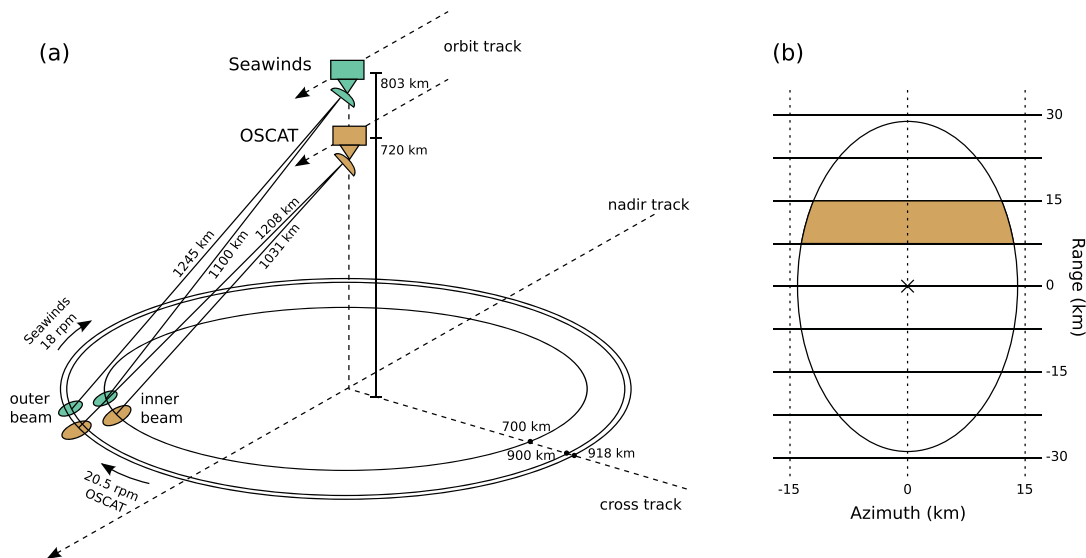


Fig. 1. (a) OSCAT and QuikSCAT orbital observation geometry. The dual-pencil-beam antenna spins about nadir as the spacecraft moves along its orbit. OSCAT is depicted in orange, and QuikSCAT is depicted in green. (b) Conceptual diagram of the OSCAT 3-dB elliptical antenna footprint with iso-range lines. The shaded area illustrates a “slice” resolution area.

TABLE I
COMPARATIVE SUMMARY OF MAJOR CHARACTERISTICS OF QUIKSCAT AND OSCAT [24]

Parameter	QuikSCAT		OSCAT	
Antenna type	Dual-feed parabolic (1.0 m diameter)		Dual-feed parabolic (1.0 m diameter)	
Orbital period	101 min (14.25 orbits/day)		99.31 min (14.5 orbits/day)	
Satellite altitude	803 km at equator		720 km at equator	
Frequency	13.402 GHz		13.515 GHz	
Wavelength	0.0224 m		0.0221 m	
Scan rate	18 rpm		20.5 rpm	
PRF (per beam)	92.5 Hz		96.5 Hz	
Start date	Jun. 19, 1999		Sep. 23, 2009	
End date	Nov. 23, 2009		—	
	Inner beam	Outer beam	Inner beam	Outer beam
Polarization	HH	VV	HH	VV
Slant range (km)	1100	1245	1031	1208
Incidence angle ($^{\circ}$)	46	54	49	57
Swath width (km)	1400	1800	1400	1836
Beamwidth (Az \times El)	$1.6^{\circ} \times 1.8^{\circ}$	$1.4^{\circ} \times 1.7^{\circ}$	$1.47^{\circ} \times 1.62^{\circ}$	$1.39^{\circ} \times 1.72^{\circ}$
Footprint (km) (Az \times El)	24.0×31.0	26.0×36.0	26.8×45.1	29.7×68.5

return echo into multiple range bins, as depicted in Fig. 1(b). Measurements of σ° corresponding to individual range bins are termed “slices.” There are a total of 7 slices reported for an inner beam echo and 12 slices reported for an outer beam echo [24]. There is a corresponding SRF associated with each individual egg and slice.

The return echo experiences a Doppler shift caused by motion and attitude of the spacecraft, azimuth position of the antenna, and rotation of the Earth. Doppler shift induced by the azimuth position of the antenna is corrected on board, while that induced by Earth’s rotation and spacecraft’s attitude is compensated by providing sufficient bandwidth for the return echo [24]. Across each slice, differential Doppler shift can cause the orientation of the SRF to vary. However, this does not affect the egg SRF. Because of complications associated with slices, estimation of slice SRF is not addressed in this paper [27].

The orientation of the Oceansat-2 orbit as well as the synchronicity of antenna rotation with PRF means that a given

spot on the Earth’s surface is observed by finite azimuthal and incidence geometries. As a consequence, regions of the Earth covered by only a few passes of the scatterometer, such as low latitude locations, exhibit very limited azimuth and incidence angle diversity. Though desirable for some applications, synchronizing the PRF with antenna scan rate additionally decreases azimuthal and incidence geometries by limiting azimuth angle looks per satellite revolution and scan frame. For SRF estimation, this can be an inhibiting characteristic which results in a bias in estimates of the SRF that is dependent on the spatial distribution of σ° measurements used in the estimate. This measurement location dependent bias results in a misshapen SRF estimate. When performing SRF estimation as outlined in this paper, care must be taken to choose a geographical sampling region at high latitudes to increase the diversity of azimuthal and incidence geometries.

During the examination of OSCAT L1B data, it was observed that there were errors in the reported locations of σ° measurements. To determine the measurement location

bias, the σ° signature of islands were used by forming high-resolution σ° SIR images of the islands using OSCAT L1B data, and then computing the distance offset from the reported geographic center of the island to the island centroid computed from the SIR images. This was exhaustively done for all possible combinations of ascending/descending, fore/aft, and H/V-pol data. Upon determination of the location bias, appropriate corrections were made for all σ° measurements used herein. Corrections to the σ° measurement locations were found to significantly improve the results of the ensuing SRF estimation method for OSCAT.

III. SPATIAL RESPONSE FUNCTION

The power P_r received by OSCAT can be decomposed into a component due to the backscattered signal P_b from the target and a noise component P_n so

$$P_r = P_b + P_n$$

where P_r is the total received power, and P_n encapsulates the noise caused by instrument electronics and atmospheric effects. The power reflected from the surface of the Earth is

$$P_b = \frac{P_t \lambda^2}{(4\pi)^3} \int_A \frac{G^2 \sigma^\circ}{R^4} dA \quad (1)$$

where P_t is the transmitted power, λ is the wavelength, G is the antenna gain, σ° is the true normalized radar backscatter of the Earth's surface, R is the slant range, and A denotes the area illuminated by the antenna [24]. Assuming that the radar backscatter is constant over the illuminated area of the target, a signal-only weighted spatial average of σ° can be derived as [23]

$$\bar{\sigma}^\circ = \frac{P_b}{X}$$

where $\bar{\sigma}^\circ$ denotes the signal-only weighted spatial average of σ° , and X is a radar calibration parameter defined as

$$X = \frac{P_t \lambda^2}{(4\pi)^3} \int_A \frac{G^2}{R^4} dA. \quad (2)$$

By combining (1) and (2), $\bar{\sigma}^\circ$ can be expressed as

$$\bar{\sigma}^\circ = \int_A h(\vec{v}) \sigma^\circ(\vec{v}) d\vec{v} \quad (3)$$

where \vec{v} represents a suitably defined coordinate system and h is the SRF. The SRF is defined by

$$h = \frac{\frac{G(\vec{v})^2}{R(\vec{v})^4}}{\int_A \frac{G(\vec{\alpha})^2}{R(\vec{\alpha})^4}} \quad (4)$$

where $\vec{\alpha}$ is a dummy variable used for integration. The SRF combines the effects of the gain and spreading loss into a normalized weighting function of σ° over the area A of the Earth illuminated by the antenna, such that

$$\int_A h(\vec{v}) d\vec{v} = 1$$

and $h(\vec{v}) \geq 0$.

Estimates \hat{P}_b of the signal-only power P_b are obtained by

$$\hat{P}_b = P_r - \hat{P}_n$$

where \hat{P}_n is an estimate of the power in the noise. The estimate of $\bar{\sigma}^\circ$ can be obtained by

$$z = \frac{\hat{P}_b}{X} = \frac{P_b + P_n - \hat{P}_n}{X} = \bar{\sigma}^\circ + N \quad (5)$$

where z represents the estimate of $\bar{\sigma}^\circ$, and N is the noise caused by the scaled error in the estimate of the noise power, defined as

$$N = \frac{P_n - \hat{P}_n}{X}.$$

The noise is characterized by the scatterometer noise model, i.e., $N \sim \mathcal{N}(0, K_p^2 \bar{\sigma}^{\circ 2})$, where K_p is the normalized standard deviation of the echo return energy, and is a function of instrument parameters and signal-to-noise ratio (SNR) [24]. In summary, (5) represents the measurement model for OSCAT, where the measured values of normalized radar backscatter reported by the satellite are noisy estimates z of the σ° weighted spatial average $\bar{\sigma}^\circ$.

IV. MATHEMATICAL FORMULATION

The measurement model for OSCAT σ° measurements is a generalized form of the convolution of σ° with the SRF h plus the additive noise N . Inverting the measurement model to solve for σ° at high spatial resolution using observations z is an important research problem in image reconstruction and remote sensing [25]. A similar, yet less commonly addressed problem is to invert the measurement model to solve for h instead. To solve for h , we use a least-squares estimation approach that takes advantage of the dense irregular sampling characteristics of satellite-borne radar while incorporating error in measurements z . A reasonable assumption is made that the SRF does not change significantly pass to pass over a small geographic region on the Earth's surface, thus allowing measurements from multiple passes of the scatterometer to be combined. We first discuss nonparametric estimates of h , followed by a method for its parametric estimation.

Other more sophisticated estimation methods were considered (e.g., least-squares in log space, total least-squares, maximum likelihood), but it was found that a straightforward least-squares approach provided good estimates with fewer complications. More sophisticated methods generally require more assumptions and have more difficulties with the intrinsic variability issues, such as errors in sampling, quantization in location, and time variations in the target and SRF. Thus, for simplicity, we adopted the least-squares approach in normal space for this paper.

A. Least Squares

To incorporate antenna rotation and orbit position into the m th measurement z_m , (3) can be rewritten as

$$z_m = \int_A h(\phi_m, \vec{x}_m, \vec{v}) \sigma^\circ(\vec{v}) d\vec{v} + N_m \quad (6)$$

where ϕ_m and \vec{x}_m are the rotation and center location of h on the surface of the Earth for the m th measurement.

Based on assumptions made in Section II, we can assume that the antenna rotation angle and the measurement location affect only the orientation of the SRF h and not its overall shape. Accordingly, shifts and rotations associated with egg measurements can be applied to the σ° field instead of h , allowing z_m to be written as

$$z_m = \int_A h(\vec{v}) \sigma^\circ(\phi_m, \vec{x}_m, \vec{v}) d\vec{v} + N_m.$$

Discretizing the inner product into a finite summation over K pixels of a σ° field grid centered about h and tangential to the Earth's surface gives

$$z_m \approx \sum_{k=1}^K h(\vec{v}_k) \sigma^\circ(\phi_m, \vec{x}_m, \vec{v}_k) \Delta v + N_m$$

where \vec{v}_k represents the K sampling locations over the SRF, \vec{x}_m is the center location of σ° for the m th measurement in kilometers north and east of the center of h , and Δv is a constant denoting the area (km^2) of each grid element. The summation can then be represented as the Euclidean inner product of vectors \mathbf{S} and \mathbf{h} for the m th measurement by

$$\begin{aligned} z_m &\approx \mathbf{S}_m^T \mathbf{h} + N \\ \mathbf{S}_m &= \begin{bmatrix} \sigma^\circ(\phi_m, \vec{x}_m, \vec{v}_1) \\ \sigma^\circ(\phi_m, \vec{x}_m, \vec{v}_2) \\ \dots \\ \sigma^\circ(\phi_m, \vec{x}_m, \vec{v}_K) \end{bmatrix} \Delta v \\ \mathbf{h} &= \begin{bmatrix} h(\vec{v}_1) \\ h(\vec{v}_2) \\ \vdots \\ h(\vec{v}_K) \end{bmatrix} \end{aligned} \quad (7)$$

where \mathbf{S} is the discretized σ° over a localized region of the Earth's surface, and \mathbf{h} is the discretized SRF. Our goal is to estimate \mathbf{h} . For M samples of z at different locations, a vector \mathbf{z} is formed as

$$\mathbf{z} = \begin{bmatrix} z_1 \\ z_2 \\ \vdots \\ z_M \end{bmatrix} \approx \begin{bmatrix} \mathbf{S}_1^T \\ \mathbf{S}_2^T \\ \vdots \\ \mathbf{S}_M^T \end{bmatrix} \mathbf{h} + \begin{bmatrix} N_1 \\ N_2 \\ \vdots \\ N_M \end{bmatrix} = \mathbf{Q}\mathbf{h} + \mathbf{e}. \quad (8)$$

This equation provides a matrix multiplicative form of the measurement model, where $\mathbf{Q} \in \mathbb{R}^{M \times K}$.

In order to invert the measurement model and recover h , the sampling criteria for z must be satisfied. The nonuniform sampling characteristics of the scatterometer complicate this. In general, the spectrum of σ° is not necessarily band-limited. However, since σ° is sampled by h , which is low-pass, the observed σ° is effectively prefiltered, minimizing high frequencies. Thus, with sufficiently dense sampling, as can be obtained by combining multiple passes, aliasing in the spectrum of z can be minimized and h can be recovered from z through inversion of \mathbf{Q} .

To ensure sufficiently dense sampling of z , measurements are collected for multiple passes over the sampling grid, resulting in $M \gg K$, such that (8) is overdetermined. A least-squares estimate $\hat{\mathbf{h}}$ can be found that minimizes the l_2 norm of

the error $\|\mathbf{z} - \mathbf{Q}\mathbf{h}\|_2^2$, such that $\hat{\mathbf{h}}$ is the optimum solution with respect to the l_2 norm. The least-squares solution is given by the Moore–Penrose pseudo-inverse of \mathbf{Q}

$$\hat{\mathbf{h}}_{\text{LS}} = \mathbf{Q}^\dagger \mathbf{z} \quad (9)$$

where $\mathbf{Q}^\dagger = (\mathbf{Q}^H \mathbf{Q})^{-1} \mathbf{Q}^H$.

Informative estimates of h require fine grid spacing and a sufficiently large region of support that provides for possible sidelobes of the SRF. However, there are tradeoffs associated with grid spacing and region of support. The first tradeoff is memory capabilities of the computing platform. Providing a sufficient region of support while trying to decrease grid spacing results in demands on system memory that may exceed capabilities. The second tradeoff pertains to potential aliasing in the spectrum of z . The grid spacing effectively acts as a low-pass filter by averaging components that fall in a similar sample. Smaller grid spacing allows for higher resolution estimates of the SRF but may be noisier and require more measurements. Larger grid spacing suppresses aliasing in SRF estimates while being more computationally friendly, but has lower resolution. To balance this tradeoff, we have chosen a grid spacing of approximately 2.225 km/pixel. Since (8) may be poorly conditioned, a robust solution can be obtained through rank reduction of \mathbf{Q} .

B. Rank-Reduced Least Squares

To improve the condition of (8), singular value decomposition (SVD) is used to replace the ill-conditioned matrix \mathbf{Q} with a reduced rank approximation. This is done by identifying and removing the numerically sensitive portion of \mathbf{Q} . Factoring (8) using SVD yields

$$\mathbf{z} = \mathbf{U} \mathbf{\Sigma} \mathbf{V}^H \mathbf{h} + \mathbf{e} \quad (10)$$

where $\mathbf{U} \in \mathbb{R}^{M \times M}$ is unitary, $\mathbf{V} \in \mathbb{R}^{K \times K}$ is unitary, and $\mathbf{\Sigma} \in \mathbb{R}^{M \times K}$ is a diagonal matrix with the singular values of \mathbf{Q} ordered down the diagonal so that

$$\sigma_1 \geq \sigma_2 \geq \dots \geq \sigma_p \geq 0$$

where $p \leq \min(M, K)$ [26].

To quell amplification of noise in the estimate of \mathbf{h} , the small singular values of \mathbf{Q} are zeroed out to obtain an approximation $\mathbf{\Sigma}_1$ of the singular value matrix $\mathbf{\Sigma}$. The rank-reduced approximation for \mathbf{Q} is obtained by rewriting (10) in block-matrix form as

$$\tilde{\mathbf{Q}} = [\mathbf{U}_1 \ \mathbf{U}_2] \begin{bmatrix} \mathbf{\Sigma}_1 & \mathbf{0} \\ \mathbf{0} & \mathbf{\Sigma}_2 \end{bmatrix} \begin{bmatrix} \mathbf{V}_1^H \\ \mathbf{V}_2^H \end{bmatrix} = \mathbf{U}_1 \mathbf{\Sigma}_1 \mathbf{V}_1^H \quad (11)$$

where $\mathbf{U}_1 \in \mathbb{R}^{M \times L}$, $\mathbf{\Sigma}_1 \in \mathbb{R}^{L \times L}$, and $\mathbf{V}_1 \in \mathbb{R}^{K \times L}$ are the respective portions of \mathbf{U} , $\mathbf{\Sigma}$, and \mathbf{V} corresponding to the first $L < p$ significant singular values of \mathbf{Q} ; and \mathbf{U}_2 , $\mathbf{\Sigma}_2$, and \mathbf{V}_2 are zero matrices corresponding to the small singular values. Solving for (10) using $\tilde{\mathbf{Q}}$ gives

$$\hat{\mathbf{h}}_{\text{SVD}} = \tilde{\mathbf{Q}}^\dagger \mathbf{z} = \mathbf{V}_1 \mathbf{\Sigma}_1^{-1} \mathbf{U}_1^H \mathbf{z} \quad (12)$$

where the inverse of $\mathbf{\Sigma}_1$ is trivial because it is a diagonal matrix.

The computational complexity of the SVD is reduced by incorporating a smaller number of significant singular values,

i.e., smaller L . Increasing L reduces the reconstruction error, but at the risk of amplifying noise in z as well as introducing noise into the reconstruction process. The optimum choice of L to minimize the reconstruction error is determined through simulation, as shown in Section VI.

While the rank-reduced least-squares technique produces satisfactory results for visualization, the solution is large and burdensome for implementation in algorithms using the SRF. Additionally, since the SRF varies over the Earth's surface depending on the location, an estimate found in a tangential plane needs to be projected into the antenna azimuth and elevation angle space for universal use. Accordingly, a parameterized estimate of \mathbf{h} in antenna azimuth and elevation angle space is sought to simplify the problem. Since, to first order, the main lobe shape and size are the most important for describing the SRF, parameterized estimation of the SRF focuses primarily on the main lobe and is not meant to model the sidelobe structure.

C. Parameterization

A parameterized estimate of \mathbf{h} for eggs can be obtained in antenna azimuth and elevation angle space using a second-order polynomial. Higher order polynomials may be used, but they may degrade performance over the main lobe through sidelobe noise introduced by higher degrees of freedom. The parameterized SRF is represented as

$$\mathbf{h} = C\mathbf{b}$$

where $C = [\zeta^2, \zeta, \psi^2, \psi, \mathbf{1}] \in \mathbb{R}^{\Psi \times 5}$, $\mathbf{b} = [b_1, \dots, b_5] \in \mathbb{R}^{5 \times 1}$, and ζ and ψ are, respectively, the azimuth and elevation angles of the antenna beam about the center of \mathbf{h} , which is defined over the Ψ grid elements of its main lobe. Inserting the parameterized definition of \mathbf{h} into (8) and solving for \mathbf{b} in the least-squares sense results in

$$\hat{\mathbf{b}} = (Q_{\Psi} D_{\Psi} C)^{\dagger} \mathbf{z}_{\Psi} \quad (13)$$

where $D_{\Psi} = \text{diag}(\Delta v_1, \Delta v_2, \dots, \Delta v_{\Psi}) / \Delta v \in \mathbb{R}^{\Psi \times \Psi}$ is a diagonal matrix composed of normalized scaling factors to account for the area of each grid element, Δv_k is the area (km^2) projected on the Earth's surface by the k th grid element defined in antenna azimuth and elevation angle space, and the Ψ denotes that the estimation is only performed over the main lobe of \mathbf{h} . Having estimated \mathbf{b} , the estimate of the SRF is then computed by

$$\hat{\mathbf{h}}_{\text{Par}} = C\hat{\mathbf{b}}. \quad (14)$$

The next section discusses construction of Q , the choice of the sampling region, and the methodology for approximating σ° .

V. GEOGRAPHIC SAMPLING REGION

Constructing the matrix Q presented in (8) requires a model for \mathbf{S} . Even though the σ° of the Earth's surface is not known exactly, good approximations can be made for regions with known geographical composition, such as islands. By selecting isolated islands that are elliptical in shape as homogeneous targets against a "dim" ocean background, \mathbf{S} can be modeled

as an ellipsoid of constant σ° over \vec{v}_i in an ocean background \vec{v}_o , where \vec{v}_i and \vec{v}_o represent the island and ocean pixels, respectively. Important to maintaining accurate SRF estimation is selecting islands at high latitude locations to ensure high diversity in azimuthal and incidence geometries, as discussed in Section II.

A. Island Targets

Advantages of island targets include simplicity and high signal-to-clutter ratio (SCR) in σ° measurements, where signal refers to the island σ° and clutter refers to the ocean σ° . High SCR is required to potentially recover information contained in the sidelobes of the SRF. In using an island model, an important consideration is the island size.

To achieve full reconstruction over the spatial main lobe of \mathbf{h} , we require that there be no nulls within the spectral region of support of the island σ° . Typically, \mathbf{h} has low-pass characteristics due to the antenna aperture, while the island σ° model used in the construction of Q exhibits a sinc-like spectrum. The wave number at which nulls in the island σ° spectrum occur is inversely proportional to the size of the island. If nulls of the island σ° spectrum lie within the spectral region of support of the main lobe of \mathbf{h} , information is irretrievably lost and full reconstruction of the main lobe of \mathbf{h} hindered. This suggests using smaller islands to push the spectral nulls outside the spectral region of support of the main lobe of \mathbf{h} . However, small islands exhibit lower SCR than large islands, thereby decreasing the effective SNR in the reconstruction of \mathbf{h} . To achieve minimum error in estimates of \mathbf{h} , an optimum island size is determined through simulation in Section VI to optimize the tradeoff between the frequency response requirement on island σ° and SCR.

B. Background σ°

Depending on the location, the ocean background may be open ocean, sea ice, or a combination of both. Ocean σ° is highly variable temporally and spatially due to weather phenomena. While season and weather phenomena can cause changes in island σ° as well, data is selected such that the island σ° is approximately constant. Temporal variability in the mean σ° of the island can be mitigated by normalizing the σ° measurements for each pass over the island. Ocean σ° , however, is less predictable and more difficult to model.

To minimize the complexity of the ocean σ° model, it is necessary to modify the problem somewhat. The original problem set forth in (8) can be decomposed into individual island and ocean components as

$$Q\mathbf{h} + \mathbf{e} = (Q_i + Q_o)\mathbf{h} + \mathbf{e} = \mathbf{z}_i + \mathbf{z}_o = \mathbf{z}$$

where i and o denote the island and ocean components, respectively, and Q_i and Q_o are disjoint matrices since $\vec{v}_i \cap \vec{v}_o = \emptyset$. By doing so, ocean σ° can be disregarded completely by simplifying the problem to

$$Q_i\mathbf{h} + \mathbf{e} = \mathbf{z} - \hat{\mathbf{z}}_o = \hat{\mathbf{z}}_i \quad (15)$$

where $\hat{\mathbf{z}}_i$ and $\hat{\mathbf{z}}_o$ are estimates of the island contribution and ocean contribution, respectively, of measurements near the

island. In this case, “near” means within about the 10-dB antenna footprint from the perimeter of the island. Thus, measurements used in the estimation are restricted to near the island to ensure a dominant land contribution. The ocean contribution \mathbf{z}_o is estimated separately for each pass using a least-squares spatially varying quadratic fit over an extended area outside the 10-dB antenna footprint. After removal of the estimated ocean contribution $\hat{\mathbf{z}}_o$ from measurements near the island, the estimation methods for \mathbf{h} can then be applied to the simplified model of (15). It is worth noting that, in applying the simplified model, erroneous estimates of the ocean contribution $\hat{\mathbf{z}}_o$ can lead to increased noise in the SRF estimation through the error $\mathbf{e}_o = \mathbf{z}_o - \hat{\mathbf{z}}_o$. To determine the extent to which \mathbf{e}_o degrades the performance of SRF estimation, a test is conducted with simulated noisy realizations of $\hat{\mathbf{z}}_o$ in Section VI.

VI. SIMULATION

Simulations are performed to validate the efficacy of the method outlined above for eggs. By comparing the reconstruction error due to simulated signal-only measurements and simulated noisy measurements, it is found that with sufficiently dense sampling (approximately 100+ revs over the Peter I island), reconstruction error due to measurement noise is insignificant compared to that due to the signal only. Thus, the remainder of this section focuses on minimizing the reconstruction error from estimates of the signal-only ($\hat{\mathbf{z}}_i$) measurements. The simulation provides a method to select the optimal island size and the number of significant singular values L that results in the minimum reconstruction error. The extent to which erroneous estimates of ocean contribution $\hat{\mathbf{z}}_o$ affects SRF estimation is also determined.

A. Simulation Procedure

Simulated signal-only measurements z_s used in the simulation procedure are constructed via the inner product of (7) without the noise term. The subscript s is used to denote a simulated quantity. A simulated SRF \mathbf{h}_s is used with center locations \vec{x} and rotations ϕ taken from the reported OSCAT H-pol cell measurements over the Peter I island ($68^\circ 50' 50''$ S, $90^\circ 35' 41''$ W) and various simulated σ° scenes \mathbf{S}_s . The matrix multiplicative form of the simulation measurement model is

$$\mathbf{z}_s = \mathbf{Q}_s \mathbf{h}_s \quad (16)$$

where \mathbf{z}_s is a vector of length M of the simulated signal-only measurements, and \mathbf{Q}_s is composed of the simulated σ° scenes corresponding to the M measurements.

The synthetic σ° scenes \mathbf{S}_s used for measurement simulation consist of elliptical islands similar in shape to Peter I Island characterized by homogeneous backscatter in a constant backscatter ocean background -30 dB down with respect to an island. The islands are constructed to be centered about the center location of the Peter I island and have an area given by $A_I = \gamma A_h$, where A_I is the area of a given island, A_h is the area of the Earth illuminated by the 3-dB response of \mathbf{h}_s , and γ is the area ratio. For

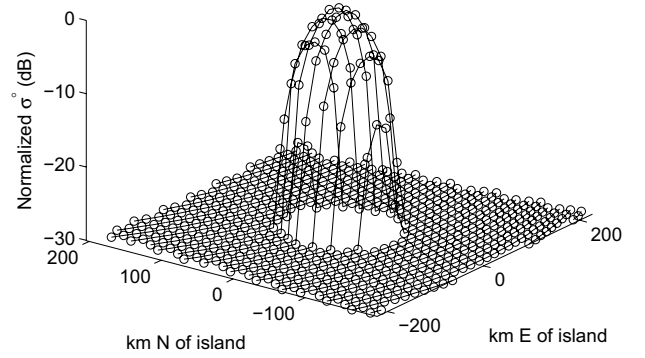


Fig. 2. Signal-only simulated measurements z_s for eggs with island size corresponding to $\gamma = 0.75$. Measurements are shown for one pass of rev 1002 over the Peter I island. Each point represents the spatial average of \mathbf{S}_s weighted by \mathbf{h}_s , and locations corresponds to the center of \mathbf{h}_s upon sampling. The measurements are normalized in the plot.

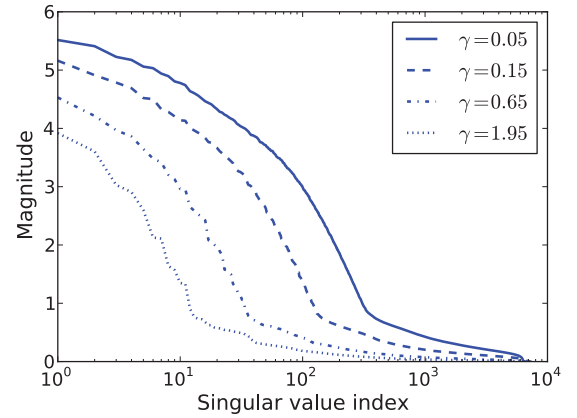


Fig. 3. Singular value curves of $\mathbf{Q}_s(\gamma)$ for the simulation. The x -axis is shown on a logarithmic scale. The singular values can be divided into two groups by the elbow in each respective curve. Generally, the upper part of the curve corresponds to the signal, and the lower part corresponds to the noise.

simulated measurements, \mathbf{h}_s is elliptical with a major-to-minor aspect ratio similar to the OSCAT H-pol footprint. A half-sinusoid is applied over \mathbf{h}_s to mimic the main lobe of a realistic SRF response. Fig. 2 shows the simulated signal-only egg measurements for $\gamma = 0.75$ during one pass over the Peter I island on rev 1002.

Estimates $\hat{\mathbf{h}}_s$ of simulated SRFs are computed using the rank-reduced least-squares method

$$\hat{\mathbf{h}}_s = \tilde{\mathbf{Q}}_s^\dagger \mathbf{z}_s. \quad (17)$$

The accuracy of $\hat{\mathbf{h}}_s$ is determined through two metrics

$$\epsilon = |B_3(\mathbf{h}_s) - B_3(\hat{\mathbf{h}}_s)|$$

$$\delta = \sqrt{\frac{1}{K} (\mathbf{h}_s - \hat{\mathbf{h}}_s)^\top (\mathbf{h}_s - \hat{\mathbf{h}}_s)}$$

where ϵ is the absolute value of the difference in mean 3-dB beam widths B_3 , and δ is the root mean square (RMS) reconstruction error. The mean 3-dB beam width B_3 is the average of 3-dB beam widths calculated at different aspect angles about the center of an individual SRF, and the reconstruction error is $\mathbf{h}_s - \hat{\mathbf{h}}_s$, where $\hat{\mathbf{h}}_s$ is first normalized to 1

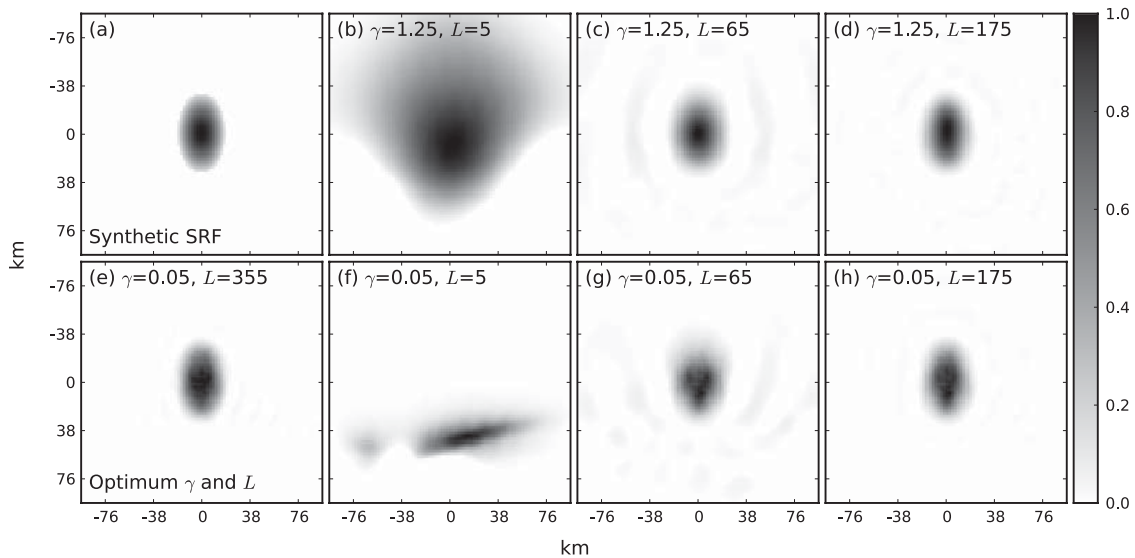


Fig. 4. Images of (a) synthetic \mathbf{h}_s , (b)–(d) its estimates $\hat{\mathbf{h}}_s(\gamma = 1.25)$, (e) its estimate $\hat{\mathbf{h}}_s(\gamma = 0.05, L = 355)$ for optimum values of γ and L , and (f)–(h) its estimates $\hat{\mathbf{h}}_s(\gamma = 0.05)$. The x - and y -axes represent kilometers in ζ and ψ , respectively, in a tangent plane at the Earth's surface. The grid spacing is approximately 2.225 km/pixel. The estimates $\hat{\mathbf{h}}_s(\gamma = 1.25)$ corresponding to (b) $L = 5$, (c) $L = 65$, and (d) $L = 175$, (e) estimate $\hat{\mathbf{h}}_s(\gamma = 0.05, L = 355)$, and estimates $\hat{\mathbf{h}}_s(\gamma = 0.05)$ corresponding to (f) $L = 5$, (g) $L = 65$, and (h) $L = 175$ are normalized to 1 by their respective maximum values.

to eliminate biases in δ as a result of the relative magnitude differences in $\hat{\mathbf{h}}_s$. The first metric ϵ can give a good sense of error in the size of $\hat{\mathbf{h}}_s$, but it offers no sense of location errors within the SRF window. The second metric δ helps to provide a sense of measurement location biases in $\hat{\mathbf{h}}_s$, while also offering a sense of size accuracy. However, without ϵ , there is some ambiguity as to whether the increase in δ is caused by error in the location or size of $\hat{\mathbf{h}}_s$. Therefore, the two metrics serve to complement each other and minimize ambiguities.

For determining the optimum values of γ and L , we use

$$\gamma, L = \arg \min_{\gamma, L} \delta(\gamma, L). \quad (18)$$

The metric ϵ is used to verify that outcomes of γ and L do not lead to significant errors in the size of $\hat{\mathbf{h}}_s$. For simulation, synthetic islands are created for $\gamma = 0.05$ to 1.95. The singular value curves of $Q_s(\gamma)$ are shown in Fig. 3 for multiple values of γ . The elbow in each curve naturally divides singular values into the signal (upper portion) and the noise (lower portion). Since higher singular value indices correspond to higher frequency information in $Q_s(\gamma)$, it is appropriate that L decreases as the nulls in the σ° spectrum of larger islands move towards lower wave numbers. For simulation, a range of $L = 5$ to 355 singular values is chosen based on the singular value curve for $\gamma = 0.05$. Extending the simulation to even higher values of L can quickly exceed available computational resources, in addition to raising the noise floor.

B. Simulation Results

Using the actual sampling geometry from L1B data for JD 309 of 2009 through JD 284 of 2011, measurements z_s are simulated and $\hat{\mathbf{h}}_s$ is computed for the entire range of γ and L . Fig. 4 shows $\hat{\mathbf{h}}_s$ computed using several values of L for the simulated SRF of $\gamma = 1.25$ and 0.05, along with \mathbf{h}_s .

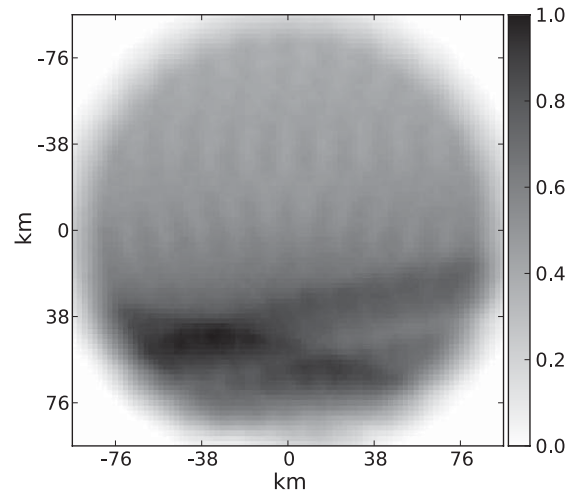


Fig. 5. Image of the normalized distribution of island measurement locations over the observation window for islands of size $\gamma = 0.15$ for \mathbf{h}_s . The x - and y -axes represent kilometers in ζ and ψ , respectively, in a tangent plane at the Earth's surface. The grid spacing is approximately 2.225 km/pixel.

The estimate $\hat{\mathbf{h}}_s$ corresponding to the optimum values $\gamma = 0.05$, $L = 355$, and $\delta(0.05, 355) = -19.82$ dB is also shown in Fig. 4. The displacement of the main lobe of $\hat{\mathbf{h}}_s$ for $L = 5$ is an artifact of the OSCAT sampling geometry of H-pol measurements over the Peter I island. Owing to the exact repeat of the Oceansat-2 satellite orbit and synchronicity of the antenna rotation angle with the PRF, there are more measurements in the lower left-hand portion of the window, causing a relative bias in SRF estimates evident in the first few singular values. Fig. 5 shows the normalized distribution of σ° locations over the observation window. The relative bias in the sample locations of $\hat{\mathbf{h}}_s$ is the primary cause of increased values of δ for $L \leq 25$, visible in Fig. 6(a). However, this has less impact on ϵ , as shown in Fig. 6(b).

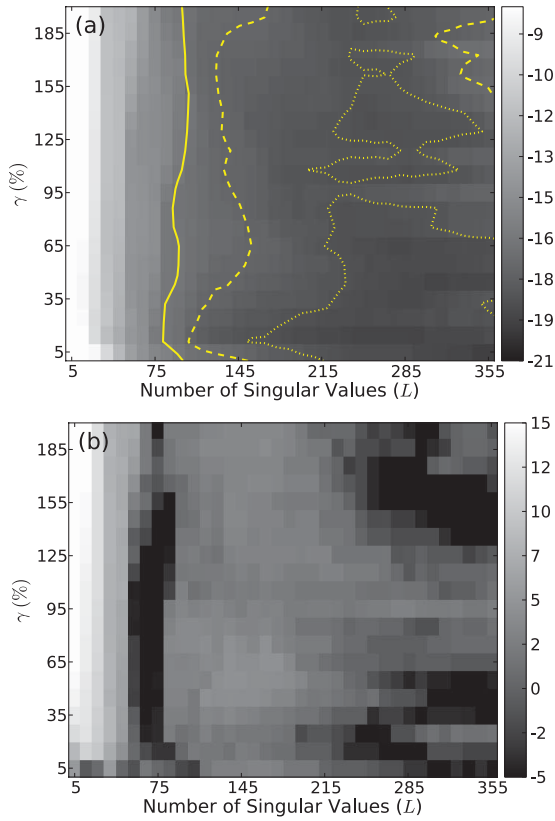


Fig. 6. Gridded images of (a) RMS reconstruction error δ and (b) absolute value of the difference ϵ of mean 3-dB beamwidths B_3 . The grids represent δ and ϵ for γ versus L . On the image of δ , the solid contour line, dashed contour line, and dotted contour line are for values within 3, 2, and 1 dB of the minimum error, respectively.

The results in Fig. 6 are obtained with perfect knowledge of the ocean contribution (a constant -30 dB down with respect to the island), meaning that perfect isolation of the signal-only contribution of \mathbf{z}_s is obtainable. However, in practice, this is not the case. For simulation, the ocean contribution estimate error e_o is approximated as spatially constant for a given pass but varying as a Gaussian random process in log space pass by pass with zero mean and variance ζ^2 . Using the simulated measurements \mathbf{z}_s for $\gamma = 0.15$, estimates $\hat{\mathbf{h}}_s$ are obtained for simulated e_o with $\zeta = \{0.25, 0.5, 1.0, 2.0, 3.0\}$ over the entire range of L . The RMS error computed between $\hat{\mathbf{h}}_s$ obtained for simulated e_o and nominal $\hat{\mathbf{h}}_s$ for each value of L is shown in Fig. 7. Even for the most extreme level of noise in simulated e_o , the RMS error in $\hat{\mathbf{h}}_s$ is no greater than -30 dB for sensible values of L .

Conclusively, the levels of error expected in $\hat{\mathbf{z}}_o$ for real-world data are not anticipated to significantly impact $\hat{\mathbf{h}}$, reaffirming the applicability of the results in Fig. 6 to OSCAT SRF estimation. However, since this simulation is performed only using the H-pol measurement geometry of OSCAT over the Peter I island, the results in Fig. 6 can serve only as a guideline for island size selection. On the image of δ , the solid contour line, dashed contour line, and dotted contour line represent values within 3, 2, and 1 dB of the minimum error. Reconstruction error can be minimized by estimating the SRF using islands and singular values corresponding to γ and L for δ values less than the contours in Fig. 6.

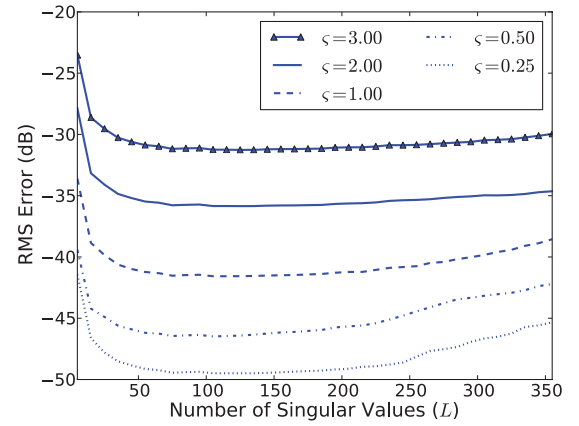


Fig. 7. Plots of the RMS error in SRF estimates $\hat{\mathbf{h}}_s$ due to ocean contribution estimation errors. The estimates $\hat{\mathbf{h}}_s$ correspond to \mathbf{z}_s for $\gamma = 0.15$ and simulated e_o for various values of ζ .

TABLE II
APPROXIMATE VALUES OF γ COMPUTED FOR PETER I AND BEAR ISLANDS USING THE OSCAT EGG FOOTPRINT DIMENSIONS FROM TABLE I

Island (Dimensions)	H-pol	V-pol
Peter I (11 \times 19 km)	0.17	0.10
Bear (12 \times 20 km)	0.19	0.11

VII. SPATIAL RESPONSE FUNCTION ESTIMATES

Options for geographical sampling regions are limited because island selection is restricted to high-latitude or polar regions. Conveniently, there are two islands close to $\gamma = 0.15$ for the egg SRF: the Peter I Island, and the Bear Island (Bjørnøya) ($74^\circ 25' 30''$ N, $19^\circ 2'$ E). Peter I and Bear islands can be closely approximated with an ellipse of dimensions 11×19 and 12×20 km, respectively. The corresponding egg γ values for the Peter I and Bear islands are given in Table II.

Because of the close proximity of the Peter I Island to the coast of Antarctica, during most of the year it is completely surrounded by sea ice. While sea ice generally exhibits consistently stronger σ° than the ocean, thereby decreasing the SCR, it is also much more temporally and spatially uniform than open ocean since ocean σ° changes with the near-surface wind. Consequently, fewer measurements are needed with a sea ice background than with an open ocean background to obtain similar estimates. On account of the limited time series of available OSCAT data, compounded with all previously mentioned constraints, we chose the Peter I Island as our focus in SRF estimation. Fig. 8 shows a QuikSCAT SIR image of the Peter I Island for JD 180-210 of 2008.

The estimation procedure is performed for individual eggs of the inner and outer beams of OSCAT using L1B measurements collected from $67^\circ 1' 48''$ S, $85^\circ 19' 48''$ W to $70^\circ 37' 48''$ S, $95^\circ 49' 48''$ W for JD 105-338 of 2011. Equation (15) is used as the measurement model to simplify implementation with actual data. Fig. 9 shows the singular value curve of Q_i

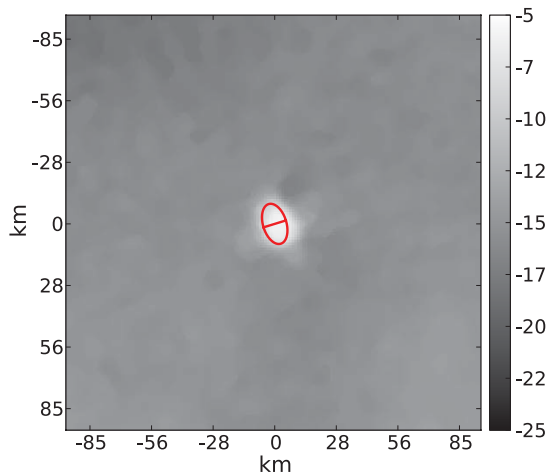


Fig. 8. QuikSCAT H-pol slice A-SIR image of the Peter I Island for JD 180-210 of 2008. The image represents σ° (in decibels) over the island using a Lambert equal-area projection with a pixel resolution of about 1.113 km/pixel. The red line traces out the elliptical approximation used for the island in estimation.

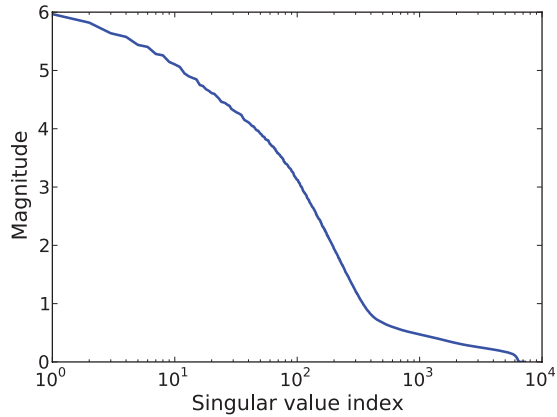


Fig. 9. Singular value curve of Q constructed for the Peter I island using H-pol egg measurements. The x -axis is shown on a logarithmic scale. The singular values can be divided into two groups by the elbow in the curve. Generally, the upper part of the curve corresponds to the signal, while the lower part corresponds to the noise.

constructed for the Peter I Island using H-pol egg measurement locations. The singular value curves for V-pol measurements are similar.

Both $\hat{\mathbf{h}}_{\text{SVD}}$ and $\hat{\mathbf{h}}_{\text{PAR}}$ are computed for the egg measurements. Fig. 10 shows $\hat{\mathbf{h}}_{\text{SVD}}$ and $\hat{\mathbf{h}}_{\text{PAR}}$ for the H-pol egg SRF computed using $L = 165$ singular values. The 3-dB beam width of the estimate is 18.1×30.6 km for the H-pol egg.

As a result of decreased SCR attributed to sea ice surrounding Peter I Island, only limited information about the sidelobes is obtainable. The 3-dB beam widths of the estimates are on the order of the reported 3-dB footprints in Table I, verifying acceptable reconstruction of the SRF over the main lobe. Two factors limiting this SRF estimation method are: 1) a short time series of available OSCAT L1B data and 2) the limited measurement geometries (antenna rotation angles). It is expected that, with a longer time series of OSCAT L1B data, better estimates are achievable using the proposed estimation procedure. A longer time series allows us to be

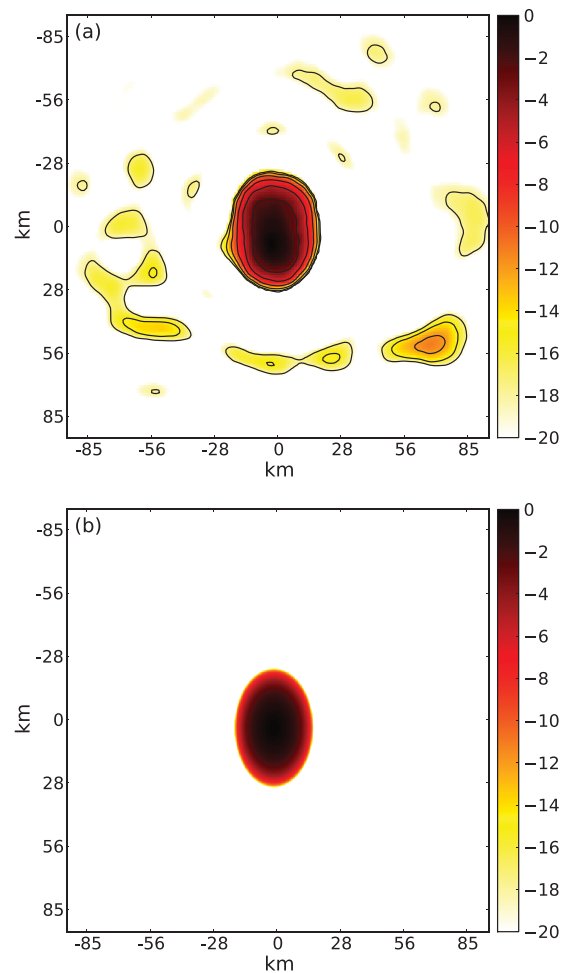


Fig. 10. Images of H-pol egg (a) $\hat{\mathbf{h}}_{\text{SVD}}$ and (b) $\hat{\mathbf{h}}_{\text{PAR}}$ computed over the Peter I Island for $L = 165$ singular values. The x - and y -axes represent kilometers in ζ and ψ , respectively, in a tangent plane at the Earth's surface. The estimates have been interpolated to a grid spacing of approximately 1.113 km/pixel and normalized to 1 by their respective maximum values for visualization. The image scale is in decibels.

more meticulous in maintaining uniformity in the ocean background while ensuring a sufficiently large number of measurements for noise suppression. Letting the orbit drift in longitude could increase the diversity of measurement geometries, thereby decreasing the possibility of locational biases in SRF estimates.

To demonstrate the utility of SRF estimation, the H-pol egg $\hat{\mathbf{h}}_{\text{PAR}}$ is used to create an H-pol egg SIR image of the Amazon basin for JD 25–26 of 2012. It is compared with a SIR image made using a simple approximation in Fig. 11, along with a QuikSCAT H-pol egg SIR image of the same region for JD 25–28 of 2009. The SRFs used to make the OSCAT SIR images are shown in Fig. 12. Though somewhat noisier than the QuikSCAT image, the OSCAT image created with $\hat{\mathbf{h}}_{\text{PAR}}$ is sharper than the image created using the approximate response. This result suggests that the new SRF provides improved reconstruction, which helps to validate the methodology presented in this paper. We note that, while we have emphasized the egg response in this paper, the general methodology can be applied to the slice response as well [27].

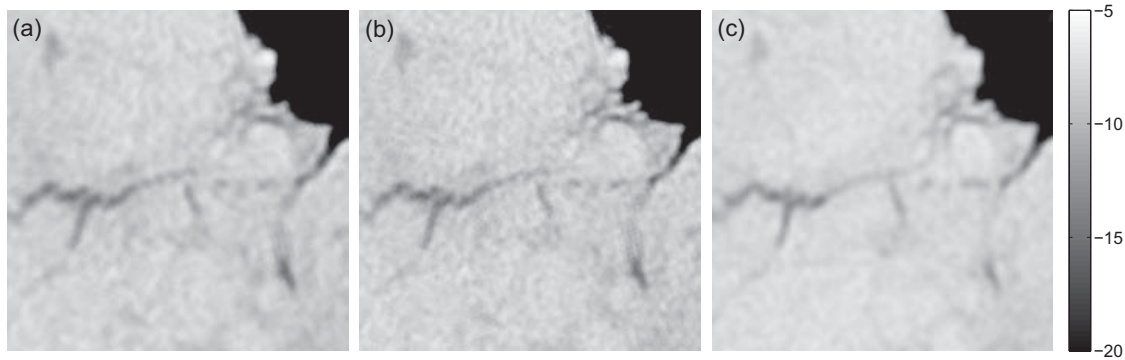


Fig. 11. OSCAT egg \mathcal{A}_h -SIR images of the Amazon basin for JD 25-26 of 2012 created using (a) current simple approximation of the SRF and (b) H-pol egg $\hat{\mathbf{h}}_{\text{par}}$. QuikSCAT egg \mathcal{A}_h -SIR image of the same region for JD 25-28 of 2009 is shown in (c) for comparison. The region shown corresponds to a box defined by (48°22' W to 57°32' W, 6°20' S to 2°50' N). The pixel resolution is approximately 4.45 km/pixel and the grayscale is in decibels.

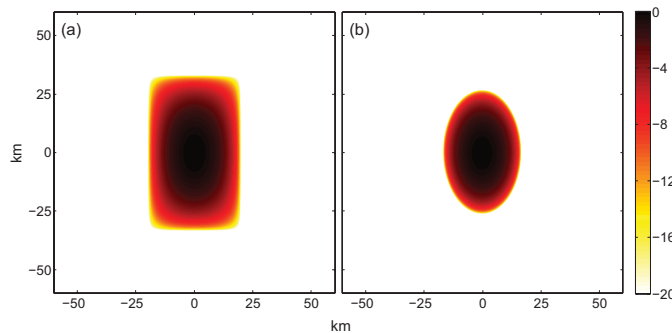


Fig. 12. Images of (a) simple approximation and (b) parameterized estimate $\hat{\mathbf{h}}_{\text{par}}$ of the H-pol egg SRF used in creating the \mathcal{A}_h -SIR images of the Amazon basin for JD 25-26 of 2012. The grid spacing is approximately 1.113 km/pixel and the peak responses have been normalized to 1 (0 dB) for visualization. The image scale is in decibels.

VIII. CONCLUSION

We have demonstrated that it is possible to estimate the SRF of OSCAT without knowing specifics of the onboard signal processing. Estimates of the SRF can be obtained by inverting the integral form of the monostatic radar equation using measured σ° over islands. The methodology for doing so has been presented, including using rank-reduced least squares for conditioning of the inversion problem and increasing computational efficiency. However, this estimation method causes the SRF estimates to be strongly dependent on both the size of the islands and the number of singular values retained. A simulation was performed to validate the efficacy of the procedure and understand the optimal choice of island size and the number of singular values. Finally, results for actual data showed that the procedure works well in practice. As a means of improving the SRF estimation procedure, future work could explore employing more sophisticated estimation methods. While developed for a pencil-beam scatterometer, the basic SRF estimation method can be applied to other radar applications, e.g., radiometers [28].

REFERENCES

- [1] W. Wagner, G. Lemoine, and H. Rott, "A method for estimating soil moisture from ERS scatterometer and soil data," *Remote Sens. Environ.*, vol. 70, no. 2, pp. 191–207, 1999.
- [2] Z. Bartalis, W. Wagner, V. Naeimi, S. Hasenauer, K. Scipal, H. Bonekamp, J. Figa, and C. Anderson, "Initial soil moisture retrievals from the METOP-A Advanced Scatterometer (ASCAT)," *Geophys. Res. Lett.*, vol. 34, no. 20, p. L20401, 2007.
- [3] V. Naeimi, K. Scipal, Z. Bartalis, S. Hasenauer, and W. Wagner, "An improved soil moisture retrieval algorithm for ERS and METOP scatterometer observations," *IEEE Trans. Geosci. Remote Sens.*, vol. 47, no. 7, pp. 1999–2013, Jul. 2009.
- [4] F. Gohin and A. Cavanie, "A first try at identification of sea ice using the three beam scatterometer of ERS-1," *Remote Sens.*, vol. 15, no. 6, pp. 1221–1228, 1994.
- [5] Q. Remund and D. Long, "Sea ice extent mapping using Ku band scatterometer data," *J. Geophys. Res.*, vol. 104, no. 11, pp. 515–527, 1999.
- [6] J. Haarpaintner, R. Tonboe, D. Long, and M. Van Woert, "Automatic detection and validity of the sea-ice edge: An application of enhanced-resolution QuikScat/SeaWinds data," *IEEE Trans. Geosci. Remote Sens.*, vol. 42, no. 7, pp. 1433–1443, Jul. 2004.
- [7] H. Anderson and D. Long, "Sea ice mapping method for SeaWinds," *IEEE Trans. Geosci. Remote Sens.*, vol. 43, no. 3, pp. 647–657, Mar. 2005.
- [8] M. Belmonte Rivas and A. Stoffelen, "New Bayesian algorithm for sea ice detection with QuikSCAT," *IEEE Trans. Geosci. Remote Sens.*, vol. 49, no. 99, pp. 1–8, Jun. 2011.
- [9] K. Stuart and D. Long, "Tracking large tabular icebergs using the SeaWinds Ku-band microwave scatterometer," *Deep Sea Res. Part II, Topical Stud. Oceanogr.*, vol. 58, nos. 11–12, pp. 1285–1300, Jun. 2011.
- [10] V. Wismann, K. Boehnke, and C. Schmullius, "Global land surface monitoring using the ERS-1 scatterometer," in *Proc. IEEE Int. Geosci. Remote Sens. Symp.*, vol. 3, Aug. 1994, pp. 1488–1490.
- [11] D. Long and P. Hardin, "Vegetation studies of the Amazon Basin using enhanced resolution Seasat scatterometer data," *IEEE Trans. Geosci. Remote Sens.*, vol. 32, no. 2, pp. 449–460, Mar. 1994.
- [12] I. Woodhouse and D. Hoekman, "Tropical forest monitoring using data from the ERS-1 Wind Scatterometer," in *Proc. IEEE Int. Geosci. Remote Sens. Symp.*, vol. 2, May 1996, pp. 845–847.
- [13] C. Emmett, R. Jensen, P. Hardin, and D. Long, "Detecting change in equatorial regions of Brazil using medium resolution satellite imagery," in *Proc. IEEE Int. Geosci. Remote Sens. Symp.*, vol. 4, Aug. 1997, pp. 1557–1559.

- [14] H. Stephen and D. Long, "Multi-spectral analysis of the Amazon Basin using SeaWinds, ERS, Seasat scatterometers, TRMM-PR and SSM/I," in *Proc. IEEE Int. Geosci. Remote Sens. Symp.*, vol. 3, Jan. 2002, pp. 1780–1782.
- [15] R. Lindsley and D. Long, "Estimating surface oil extent from the deep water Horizon Oil Spill using ASCAT Backscatter," in *Proc. IEEE Radar Con.*, May 2011, pp. 559–563.
- [16] W. Liu, "Progress in scatterometer application," *J. Oceanogr.*, vol. 58, no. 1, pp. 121–136, 2002.
- [17] M. Bourassa, H. Bonekamp, P. Chang, D. Chelton, J. Courtney, R. Edson, J. Figa, Y. He, H. Hersbach, K. Hilburn, Z. Orana Jelenak, K. A. Kelly, R. Knabb, T. Lee, E. J. Lindstrom, W. Timothy Liu, D. G. Long, W. Perrie, M. Portabella, M. Powell, E. Rodriguez, D. K. Smith, V. Swail, and F. J. Wentz, "Remotely sensed winds and wind stresses for marine forecasting and ocean modeling," *Proc. OceanObs' 09, Sustain. Ocean Observat. Inf. Soc.*, 2010, pp. 1–17.
- [18] W. Hullinger and D. Long, "Mitigation of sea ice contamination in QuikSCAT wind retrieval," *IEEE Trans. Geosci. Remote Sens.*, vol. 37, no. 2, pp. 4848–4854, Feb. 2012.
- [19] D. Long, P. Hardin, and P. Whiting, "Resolution enhancement of spaceborne scatterometer data," *IEEE Trans. Geosci. Remote Sens.*, vol. 31, no. 3, pp. 700–715, May 1993.
- [20] M. Owen and D. Long, "Land-contamination compensation for QuikSCAT near-coastal wind retrieval," *IEEE Trans. Geosci. Remote Sens.*, vol. 47, no. 3, pp. 839–850, Mar. 2009.
- [21] M. Owen, K. Stuart, and D. Long, "Ultra-high-resolution near-coastal wind retrieval for QuikSCAT," *Proc. SPIE*, vol. 6880, Sep. 2007.
- [22] K. Stuart and D. Long, "Iceberg size and orientation estimation using SeaWinds," in *Proc. IEEE Int. Geosci. Remote Sens. Symp.*, Jan. 2010, pp. 2394–2397.
- [23] I. Ashcraft and D. Long, "The spatial response function of SeaWinds backscatter measurements," *Proc. SPIE*, vol. 5151, pp. 609–618, 2003.
- [24] K. Padia and S. D. Team, "Oceansat-2 Scatterometer algorithms for sigma-0, processing and products format," in *Proc. Adv. Image Process. Group, Signal Image Process. Area, Space Appl. Centre*, Apr. 2010, pp. 1–8.
- [25] D. Early and D. Long, "Image reconstruction and enhanced resolution imaging from irregular samples," *IEEE Trans. Geosci. Remote Sens.*, vol. 39, no. 2, pp. 291–302, Feb. 2001.
- [26] T. Moon and W. Stirling, *Mathematical Methods and Algorithms for Signal Processing*, vol. 13. Upper Saddle River, NJ, USA: Prentice Hall, 2000.
- [27] J. Bradley, "Extending the QuikSCAT data record with the Oceansat-2 scatterometer," M.S. thesis, Dept. Electr. Comput., Brigham Young Univ., Provo, UT, USA, 2012.
- [28] B. Gunn, "Scatterometer image reconstruction tuning and aperture function estimation for the advanced microwave scanning radiometer aboard the Earth observing system," M.S. thesis, Dept. Electr. Comput. Eng. Brigham Young Univ., Provo, UT, 2010.



Joshua P. Bradley received the B.Sc. and M.S. degrees in electrical engineering from Brigham Young University (BYU), Provo, UT, USA, in 2010 and 2012, respectively.

He was with the BYU Microwave Earth Remote Sensing Laboratory from 2009 to 2012. He is currently with Artemis, Inc., Spanish Fork, UT, USA. His current research interests include scatterometry and synthetic aperture radar.



David G. Long (S'80–SM'98–F'08) received the Ph.D. degree in electrical engineering from the University of Southern California, Los Angeles, CA, USA, in 1989.

He was with NASA's Jet Propulsion Laboratory (JPL), Pasadena, CA, USA, from 1983 to 1990, where he developed advanced radar remote sensing systems and was the Project Engineer on the NASA Scatterometer (NSCAT) project which flew from 1996 to 1997. He also managed the SCAN-SCAT project, the precursor to SeaWinds which was launched in 1999 on QuikSCAT and 2002 on ADEOS-II. He is currently a Professor with the Electrical and Computer Engineering Department, Brigham Young University, Provo, UT, USA, where he teaches upper division and graduate courses in communications, microwave remote sensing, radar, and signal processing, and is the Director of the BYU Center for Remote Sensing. He is the Principle Investigator on several NASA-sponsored research projects in remote sensing. He has authored over 400 papers in signal processing, radar scatterometry, and synthetic aperture radar. His current research interests include microwave remote sensing, radar theory, space-based sensing, estimation theory, signal processing, and mesoscale atmospheric dynamics.

Dr. Long was the recipient of the NASA Certificate of Recognition several times. He is an Associate Editor for the IEEE GEOSCIENCE AND REMOTE SENSING LETTERS.